Chapter 5   Experiment and Theory on Micro Electronic and Macro Optical Parameters of the ITO Films

Since the refraction index (n)[1], the extinction coefficient (κ)[2], the free carrier density (n_c) [3] and the carrier mobility (μ)[4] of the ITO films are important criteria to describe the characteristics, microstructure and physical properties of the films, their studies are discussed in this chapter.

5.1. Experimental measurements of the carrier concentration (n_c) and carrier mobility (μ) of the films

5.1.1. The n_c, μ and ρ of the films as a function of thickness (d)

The carrier concentration (n_c), carrier (or Hall) mobility (μ) and resistivity (ρ) of the ITO films with different thicknesses were measured. The films were deposited at room temperature (RT) with 2.1×10^{-1} Pa total pressures (P_T) and 10% ratio of oxygen partial pressure (P_{O2}). Van der Pauw and Hall Effect measurements were used to determine carrier concentration (n_c) and carrier mobility (μ). Table 5-1 and Fig. 5-1 show ρ, n_c and μ of the ITO films for different thicknesses (d). The resistivity increased with increasing thickness except for sample h2 that reached a lower value of 5.35×10^{-4} Ωcm for 282 nm thickness. The increase of resistivity is due to the decrease in both n_c and μ with increasing thickness, except in the case of sample h2 in which μ increases. It is suggested that n_c has a very small decrease with increasing pore or swelling structure of the films when it is deposited in a longer time. This result is confirmed by our transmittance and SEM studies in Section 4.5 (Chapter 4). Because the amount of pores (or defects) in the sample h2 is little, which decreases scattering of the charge carriers, the mobility of the sample h2 increases to 17.7 cm^2/V•s. From the decrease of the carrier mobility of films from sample h3 to h4, we deduce that the amount of defects increase with the increasing thickness of the films. The lower value 14.1 cm^2/V•s mobility of sample h1 is due to a smaller amount of pore or defects than sample h2. This shows that the physical properties of thin films are different from the bulk ones. The value of mobility and carrier concentration is very sensitive to the structure of the films.

From the results presented in chapter 4, the film electrical properties show a dependence on the deposition conditions and treatment methods. Since the carrier concentration and Hall mobility (Table 5-1) maintain their magnitudes, we conclude that the better sheet resistance (R_s) of the films is due to the thickness increase ($R_s = \rho/d$, d is the thickness of a thin film, Section 3.9).

Table 5-1. The ρ, n_c and μ of the ITO films as a function of thickness, which were deposited at RT with 2.1×10^{-1} Pa P_T and 10% P_{O2}.

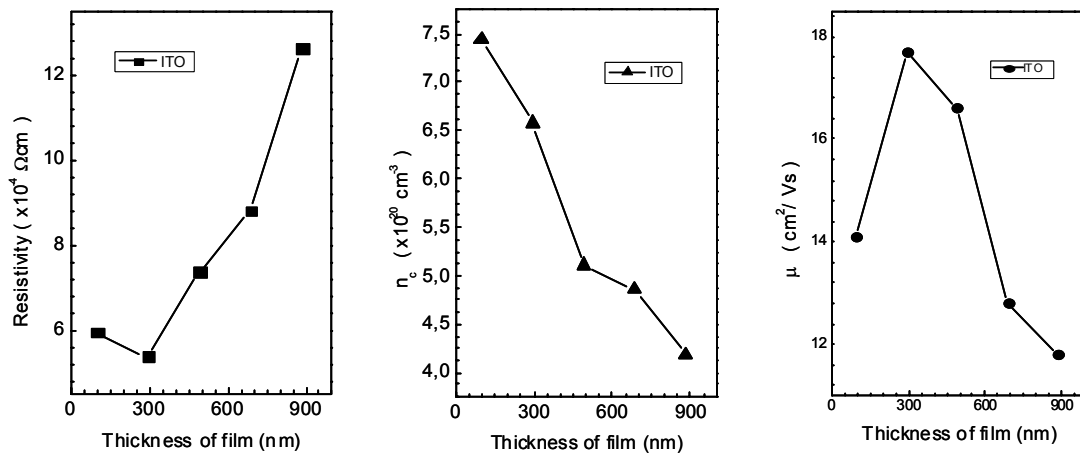| Sample	ρ (Ωcm)	n_c (cm^{-3})	μ(cm^2/V•s)	d (nm)
h1	5.93×10^{-4}	7.44×10^{20}	14.1	97
h2	5.35×10^{-4}	6.58×10^{20}	17.7	282
h3	7.34×10^{-4}	5.11×10^{20}	16.6	470
h4	1.26×10^{-3}	4.18×10^{20}	11.8	846

Fig. 5-1. The resistivity (ρ), carrier concentration (n_c) and carrier (or Hall) mobility (μ) of the ITO films as a function of thickness for films deposited at RT with 10% P_{O2}.

5.1.2. The n_c, μ and ρ of the films for different P_{O2}

The resistivity (ρ), carrier concentration (n_c) and carrier (or Hall) mobility (μ) of the ITO films were measured. The films were deposited at RT in 2 minutes, 2.1×10^{-1} Pa P_T and different P_{O2} sputtering atmosphere. Table 5-2 and Fig. 5-2 show ρ, n_c and μ of the ITO films with different P_{O2}.

The lower values of the resistivity of these ITO films are 5.93×10^{-4} and 6.01×10^{-4} Ω cm for 10% and 12% P_{O2}. Other ρ values are 9.39×10^{-4} for 2% P_{O2} and 9.12×10^{-2} Ωcm for 16% P_{O2}, respectively. Obviously an increase of ρ on either side of the optimum 10% P_{O2} was observed. The increase of resistivity is mainly due to the decrease in n_c, except for sample i2. Similar to Section 4.2.2 of Chapter 4, at less than optimum 10% P_{O2} the higher ρ obtained could be explained by the phases of metal oxide other than In_2O_3 doped SnO_2. At higher than the optimum 10% P_{O2} the larger ρ could be due to i). Additional oxygen is accumulated at the grain boundaries which could then acts as scattering centre for electrons; ii). Swelling structure of the film changes the carrier concentration (n_c).

Table 5-2. The ρ, n_c and μ of the ITO films for different P_{O2}, which were deposited at RT in 2 minutes and 2.1×10^{-1} Pa P_T.

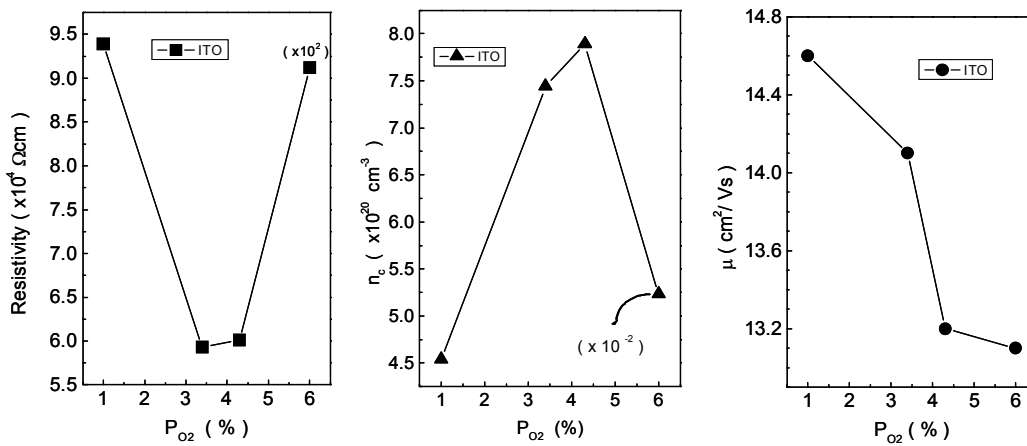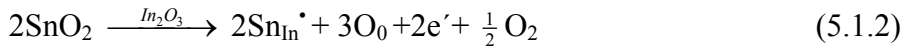| Sample	ρ (Ωcm)	n_c (cm^{-3})	μ(cm^2/V•s)	P_{O2}	d_e (nm)
i1	9.12×10^{-2}	5.23×10^{18}	13.1	16%	47.9
i2	6.01×10^{-4}	7.89×10^{20}	13.2	12%	93.9
i3	5.93×10^{-4}	7.44×10^{20}	14.1	10%	90.5
i4	9.39×10^{-4}	4.54×10^{20}	14.6	2%	66.2

Fig. 5-2. The resistivity (ρ), carrier concentration (n_c) and carrier (or Hall) mobility (μ) of the ITO films as a function of P_{O2}, deposited at RT in 2 minutes.

ITO is an n-type semiconductor, from measurements of Hall effect. The conductivity comes from the oxygen vacancies and the presence of a tin dopant which has a higher

valence than indium. Generation of n-type charge carriers such as electrons can be described as follows:

$$O_2 \rightarrow V_o^{\bullet\bullet} + 2e' + \tfrac{1}{2}O_2 \tag{5.1.1}$$

$$2SnO_2 \xrightarrow{\;In_2O_3\;} 2Sn_{In}^{\bullet} + 3O_0 + 2e' + \tfrac{1}{2}O_2 \tag{5.1.2}$$

If there is no oxygen in the deposition chamber during sputtering, the high energetic particles may knock out oxygen atoms, resulting in reduction in the film. The decrease of oxygen content enhances the presence of oxygen vacancies in the films. The oxygen vacancies act as doubly ionized donors and contribute two electrons to electrical conduction in Equ. (5.1.1). Hence, the carrier concentration increases with decreasing oxygen content from 16% to 12% P_{O2}. The increase of P_{O2} also enhances the pore in the film and hence the mobility of the carrier is lower at high P_{O2}, from 2% to 16%, especially for sample i1.

5.1.3. The n_c, μ and ρ of the films for different annealing temperatures (T_a)

The ρ, n_c and μ of the ITO films were measured. The films were deposited at 2.1×10^{-1} Pa total pressure (P_T), 10% P_{O2}, different deposition time and different annealing temperatures. Table 5-3 shows the detailed data. The resistivities (ρ) of sample j1 and j3 reach lower values of 6.40×10^{-4} and 5.93×10^{-4} Ωcm. The mobility increases up to a maximum value of 22.8cm^2/V•s after annealing at 200 ^{0}C (sample j3). The high value of sample j3 is due to the increase in grain size and lower grain boundary scattering in the annealed films. These experimental results confirm the data of the annealing effect of the films (Section 4.6 and 4.7).

Table 5-3. The n_c, μ and ρ of the ITO films for different annealing temperatures, which were deposited at 2.1×10^{-1} Pa P_T, 10% P_{O2} and different deposition time.

Sample	ρ (Ωcm)	n_c (cm^{-3})	μ(cm^2/V•s)	T_a(^{0}C)	T_d
j1	5.93×10^{-4}	7.44×10^{20}	14.1	25	2 Min.
j2	1.12×10^{-3}	5.36×10^{20}	10.4	100	4 Min.
j3	6.40×10^{-4}	4.28×10^{20}	22.8	200	4 Min.
j4	1.62×10^{-3}	1.06×10^{21}	3.63	300	18 Min.

5.2. Calculation of Optical Parameters by Using the Diffuse Reflectance Spectrum

It has been found that the film transmittance increases with increasing P_{O2} [5]. This may be caused by two reasons. One is the variation of the refractive index (n), another is the variation of the extinction coefficient (κ). In section 4.5.3 it has presented the study on the refractive index (n) calculated by interference effects. Meng et. al. studied the dispersion of n of the tin oxide films prepared at different total pressure and P_{O2}, using the transmission spectra [6]. The theoretical and experimental study of the extinction coefficient (κ) will be given in the following sub-section.

5.2.1. "Scattering" model and extinction coefficient (κ)

In the classical theory, the loss of light in passing through optical films can be caused by two factors, absorption and scattering. If the optical energy band gap E_g of the films is very high, the absorption can be neglected in the visible region. Since the optical energy band gap of the ITO films is up to 3.87 eV (Chapter 4), the light scattering is the dominant factor in the loss of light.
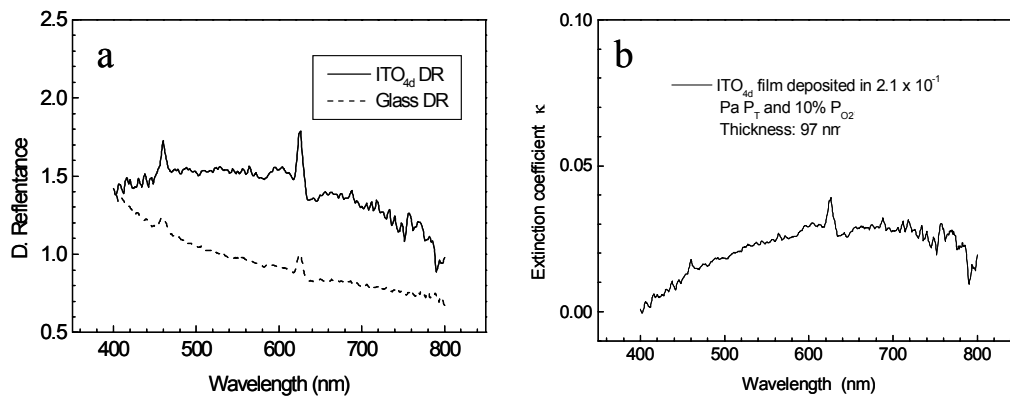

Fig. 5-3. (a) Diffuse reflectance spectra of the ITO (h1) film and the glass substrate. (b) κ variation of the sample h1 as a function of wavelength.

There are several possible scattering centres in the films. They are impurities, grain boundaries and oxygen vacancies. Since all these scattering centres are small compared with the wavelength, light scattering is of the Rayleigh type [7]. The scattering coefficient is defined as $\alpha_s = W_s/I_i = C/\lambda^4$ [8-9] and the scattering power (scattering light intensity) is $W_s = C\ I_i\ /\lambda^4$, where I_i is the irradiance intensity of light, C is a constant and λ is the

wavelength. The inverse of α_s is the e-folding distance (or skin depth), the distance over which the irradiance of light propagating in an unbounded medium decreases by a factor of e [9]. According to the Swanepoel´s theory [10] and Section 3.6, the extinction coefficient (κ) can be written as $\kappa= \alpha_e\lambda/4\pi$. Under the "scattering" model and neglecting the absorption (α_a) as discussed above, $\alpha_e=\alpha_s+\alpha_a=\alpha_s$, where α_e is the extinction loss. From the above equations, $\kappa =\alpha_e\lambda/4\pi = C/4\pi\lambda^3$. In order to change the expression of W_s to percentage (%) form, W_s was multiplied by 10^{-2} in the equation. Since I_i is defined as 100 in spectrum measurement:

$$\kappa =\lambda \bullet(10^{-4}\bullet W_s)/4\pi \qquad\qquad (5.2.1)$$

Using equation (5.2.1) the extinction coefficient k can be obtained. The diffuse reflectance and the κ values of the sample h1 are shown in Fig. 5-3 (a, b). They are also confirmed by ellipsometric measurements presented in Section 5.2.2.

5.2.2. Measurements of n and κ using ellipsometric measurements

In order to get the dispersion curves of the refractive index n and the extinction coefficient k, the ellipsometric measurements can also be used. The ellipsometric spectra were fitted using the Lorentz oscillator model (classical model). The film thickness was obtained (Table 4-2-1 and Table 4-4-1) by fitting the ellipsometric spectra and has been confirmed by SEM measurements. The fittings were done by using a Levenberg–Marquardt least squares routine[11]. The film thickness was obtained by fitting the transmittance. A small difference of thickness obtained by different methods may result from the surface top layer of the films, as the ellipsometric spectra are sensitive to it [14-15].

The dispersions of n and k of the films (thickness less than 100 nm) prepared with 2.1×10^{-1} Pa P_T and different P_{O2} are shown in Fig. 5-4. The n and k values of the films over a wavelength range of 400 nm -800 nm were plotted against the photo-energy (3.2 eV-1.4 eV). It can be seen that the sample prepared at high P_{O2} shows a different behaviour compared to the samples prepared at low P_{O2}. This can be related with the variation of the structure of the films.

The k of sample h1 at the wavelength 700 nm is 0.034 using ellipsometric measurements (Fig. 5-4b) and 0.032 by using the diffuse reflectance (Fig. 5-3b). Clearly, the results obtained by the "scattering model" and Ellipsometric measurement are in agreement in magnitude. This proves that both methods are suitable for measuring and calculating the optical and electrical parameters of the ITO films.
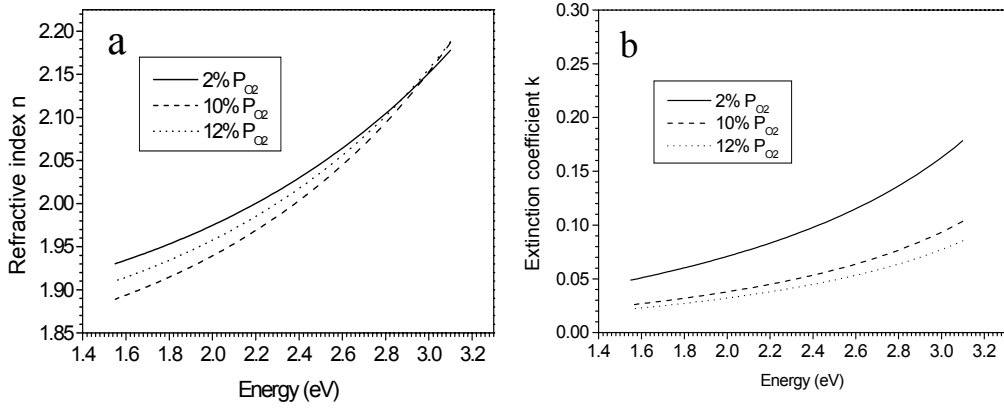
Fig. 5-4. Refractive index *n* (a) and extinction coefficient *k* (b) are in the range 400 nm-800 nm (3.2 eV-1.4 eV). The ITO films were prepared with different oxygen partial pressures.

5.3. Calculation of the Carrier Concentration n_c and Carrier Mobility μ

The transmission spectrum of an ITO film can be divided into different regions as mentioned in Section 3.6. In the visible region α_a=0, free electrons play an important role in the optical performance of the ITO films. This can be used in order to determine the parameter n_c and μ. In the strong and medium absorption region (short wavelength range) the absorption α_a value is bigger and the optical behavior of the ITO films is dominated by absorption from the valence electrons. This can be used in order to determine the energy band gap E_g.

The complex dielectric constant $\acute{\varepsilon}$ and the complex index of refraction ñ are two very important parameters to describe the electrical and optical properties in transparent thin films. Normally they can not be obtained by only one experiment. Similarly ε', ε", n, k and n_c and μ are also not obtained by one experiment (or measured directly). However there are relations between them. In the following we introduce the equation by which the optical data can be obtained from the electrical measurements of the film. Oppositively the electrical data can also be obtained from the optical measurements of the films.

According to the basic relations ñ =n+iκ and $\acute{\varepsilon}$ = ε'+ iε" = ñ^2. A relation between the dielectric function and photo-energy is derived by applying the Drude theory [5, 9, 12]:

$$\varepsilon' = \varepsilon_\infty - \frac{\omega_\rho^2}{\omega^2 + \omega_\gamma^2} = n^2 - \kappa^2 \tag{5.3.1}$$

82

$$\varepsilon" = \frac{\omega_\gamma \omega_\rho^2}{\omega(\omega^2 + \omega_\gamma^2)} = 2\kappa n \qquad (5.3.2)$$

where ε_∞ is the residual dielectric constant due to the ion core; ε' and ε'' are the real and imaginary part of the complex dielectric function $\acute{\varepsilon}$; n and κ are the real and imaginary part of the complex index of refraction ñ; ω is the photo energy; ω_ρ is the plasma frequency (or screen plasma frequency) and ω_γ is a collision frequency {relaxation energy: $(\omega_\gamma h/2\pi)^2$} or the frequency at which the free carries are scattered. The n_c and the μ can finely be determined as

$$n_c = \frac{\varepsilon_0 m^* \omega_\rho^2}{e_0^2} \qquad (5.3.3)$$

$$\mu = \frac{e_0}{m^* \omega_\gamma} \qquad (5.3.4)$$

Where ε_0 is the permittivity of free space, and e_0 the electron charge.

Kostlin et al. have discussed the ε_∞ and the effective electron mass m* of the carriers in the conduction band [13]. From his results, assuming a constant effective electron mass m* = 0.3 m_0 (m_0 the free electron mass) and ε_∞ = 4 for all samples. Therefore ε', ε'', n_e, μ, $R_{s,}$ ω_ρ and ω_γ can be calculated, and it is possible to compare the calculation from the above relations with the experimental results. The detail data it is presented in Table 5-4 and in the following paragraph.

For the sample h4 the experimental values of n_c and μ are 4.18×10^{20} (cm^{-3}) and 11.80(cm^2/V•s). The calculated value of n_c and μ is 1.54×10^{21} (cm^{-3}) and 1.21 (cm^2/V•s) at 540 nm ($\omega = 2\pi\nu = 2\pi C/\lambda = 3.47 \times 10^{15}$ S^{-1}, C is the speed of light). The calculated n= 1.89, κ=0.17, ω_ρ = 4.04×10^{15} m^{-1} and ω_γ= 4.85×10^{15} m^{-1} were obtained by using the Mathematica-4.1 Software.

From equations (5.3.1) and (5.3.2), we obtain

$$4 - \frac{\omega_\rho^2}{(3.47x10^{15})^2 + \omega_\gamma^2} = 1.89^2 - 0.17^2 \qquad (5.3.5)$$

$$\frac{\omega_\gamma \omega_\rho^2}{3.47x10^{15}(3.47^2 x10^{30} + \omega_\gamma^2)} = 2x1.89x0.17 \qquad (5.3.6)$$

After determining the solution of the equations we put the obtained results of ω_ρ = 4.04×10^{15} m^{-1} and ω_γ= 4.85×10^{15} m^{-1} into equations (5.3.3) and (5.3.4). The obtained data are

listed on Table 5-4.

Similarly, for sample j4 the direct experimental measurement of n_c and μ are 1.06 $\times 10^{21}$ (cm^{-3}) and 3.63(cm^2/V•s). The calculated values of n_c and μ are 2.04 x 10^{21}(cm^{-3}) and 2.84 (cm^2/V•s) at 540 nm. The calculated n= 1.65, κ=0.24, ω_ρ= 4.65 x 10^{15} m^{-1} and ω_γ= 2.06 x 10^{15} m^{-1} were obtained by using the Mathematica-4.1 Software. These values are in agreement in magnitudes.

Table 5-4. n_c and μ values of the ITO films

Samp.	n_c (cm^{-3})	μ(cm^2/V•s)	T_a(^{0}C)	Note
h4	4.18x10^{20}	11.80	-	Exp.
j4	1.06x10^{21}	3.63	300	Exp.
h4	1.54x10^{21}	1.21	-	Calc. n: 1.89, κ: 0.17, ω_ρ: 4.04x10^{15}m^{-1}, ω_γ: 4.85x10^{15}m^{-1}
j4	2.04x10^{21}	2.84	300	Calc. n: 1.65, κ: 0.24, ω_ρ: 4.65x10^{15}m^{-1}, ω_γ: 2.06x10^{15}m^{-1}

Note: Exp.: experiment; Calc.: calculation.

5.4. Summary of the Chapter

The refractive index (n), the extinction coefficient (κ), free carrier density (n_c) and the carrier mobility (μ) of the ITO films were studied. The n_c, μ and ρ of the ITO films with different deposition time (thickness), P_{O2} and annealing temperature were measured.

The variation of the resistivity of the ITO films is due to the combined effect of changes in the parameters n_c and μ. In case of very thin film with thickness less than 400 nm, the films can have good conductivity due to the increasing of thickness, but the n_c and μ changed for different film thickness. These show that the physical properties of the thin films are different from the bulk. The mobility and carrier concentration are very sensitive to the structure variation of the films.

The calculated optical parameter- extinction coefficient (κ) was obtained from the diffuse reflectance using "scattering model". In addition the Swanepoel method (see section 3.6) was used in order to obtain the refractive index. The Lorentz oscillator classical model has also been used for fitting the ellipsometric spectra in order to obtain the n and κ values. Clearly the results of the "scattering model" and Ellipsometric method agree in magnitude. The films prepared at different oxygen partial pressure show

different refractive index and extinction coefficient.

Through an equation that relates the dielectric function and photo-energy (Drude theory), the expression of the free carrier density (n_c) and the carrier (Hall) mobility (μ) are given. The electrical characteristics n_c and μ were compared and studied by experimental measurements and calculations using Mathematica-4.1 software. Both measured and calculated values coincide in magnitude.

5. 5.   References

[1]   Bi-Shiou Chiou and Jen-Huan Tsai, Antireflective coating for ITO films deposited on glass substrate, Journal of Materials Science: Materials in Electronics, 10(7) (1999) 491 – 495

[2]   M. Martino, A. Luches, M. Fern´andez, P. Anobile and V. Petruzzelli, Characterization of thin indium tin oxide films deposited by pulsed XeCl laser ablation, J. Phys. D: Appl. Phys. 34 (2001) 2606–2609.

[3]   A. G. Manoj, A. A. Alagiriswamy, and K. S. Narayan, Photogenerated charge carrier transport in p-polymer n-polymer bilayer structures, Journal of Applied Physics, 94(6) (2003)4088-4095.

[4]   Yutaka Ohmori, Norio Tada, Masayoshi Yoshida, Akihiko Fujii and Katsumi Yoshino, Carrier transport in a three-layered electroluminescent device, J. Phys. D: Appl. Phys. 29 (1996) 2983–2987.

[5]   M. Bender, W. Seelig, C. Daube. H. Frankenberaer . B. Ocker. J. Stollenwerk, Thin Solid Films 326 (1998) 72-77.

[6]   L.J.Meng, and M.P.Santos, Vacuum, 45(12) (1994) 1191

[7]   I. Fanderlik, Optical Properties of Glass, Elsevier, Amsterdam, 1983

[8]   H. C.Van Hulst, Light Scattering by Small Particles, Wiley, New York, 1957.

[9]   Michael Bass, Handbook of Optics, McGraw-Hill, Inc. (USA), (1995) I-6.4, 6.5, II-35.2.

[10]   R.Swanepoel, J. Phys. E, 16 (1983) 1214

[11]   Li-Jian Meng, Eddie Crossan, Andrei Voronov and Frank Placido, Indium–tin-oxide thin film prepared by microwave-enhanced d.c. reactive magnetron sputtering for telecommunication wavelengths, Thin Solid Films 422(1-2) (2002) 80-86.

[12]   C. H. L. Weihtens and P.A.C. Van Loon, Thin Solid Films, 196 (1991) 1.

[13]   H. Kostlin, R. Jost and W. Lems, Phys. Status Solidi A, 29 (1975) 87.

[14]   Šikola T., Spousta J., Strasky M., Ellipsometry and trasport studies of thin-film metal nitrides, Thin Solid Films, vol. 332, 2005

[15]   Čechal J., Tichopadek P., Nebojsa A., Bonaventurova O., Urbanek M., Spousta J., Navratil K., Šikola, T., In situ analysis of PMPSi by spectroscopic ellipsometry and XPS, Surface and Interface Analysis, vol.38 (2004) 8

Chapter 6　Bilayer Films of Ultrasonic Dipped Cadmium Sulfide and d.c. Sputtered Indium Tin Oxide

6.1. Introduction

Cadmium sulfide (CdS) and CdS/ITO (indium tin oxide, In_2O_3 doped SnO_2) bilayer films are n-type semiconductor. They act as a window material and are promising candidates for producing high efficiency photovoltaic (PV) solar cells [1-3]. Recently the bilayer films have also shown potential for applications in electrochromic devices (ECDs) [4], display screens and many other functional films [5]. A self-powered electrochromic (EC)-smart window with no external wiring and power source would be the most desirable option. An integrated PV powered EC window or combined PV and EC device is the obvious choice, particularly because PV technology is making a strong inroad in building facades. Moreover the operational characteristics of PV and EC technology are mutually compatible [6]. Papaefthimiou et al [4] have developed a good multi-layer ZnS/Ag for advanced ECD applications. CdS (or Cd) and ZnS (Zn) have similar chemical and physical properties. CdS films doped with Ag (or Hg, In, Cu) were used in different devices by various methods [5, 7]. In addition, most of the transparent conducting oxides (TCOs) have continuous edge sharing octahedral of either one or some combination of Cd^{+2}, In^{+3}, and Sn^{+4}, a key structural feature that Shannon *et al* found is common to TCOs [8]. The $Cd_{1+x}In_{2-2x}Sn_xO_4$ and CdO-In_2O_3-SnO_2 ternary systems are probably the best TCOs [9]. All these, plus some deposition advantages, such as easy process, large area and low cost prompted the present investigation of CdS/ITO bilayer films.

A great deal of research has been done in an attempt to manufacture and characterize UFP (ultrafine particles) cadmium sulfide film, because they have physical properties that are intermediate between those corresponding to the molecules and bulk material [10-11]. In order to facilitate a practical use and theoretical approaches, one inevitably encounters some very intractable problems: (i) How to make macroscopic amounts of stabilized and characterized UFP; (ii) How to control the average size of the particles and obtain a narrow distribution of sizes; (iii) How to control the shape of the particles in the UFP films; (iv) How to obtain a wider transmission range and a higher transmittance to act as the window material in a solar cell and counter electrode or ion-storage layer in ECDs.

One of the possible ways to solve these problems simultaneously is to restrict the reaction space in which the particles are created. This has been done using various methods and templates such as colloid chemistry [12], electrochemistry[13] , UFP accommodated by organic molecules [14,15], porous glasses[16], zeolites [17], synthetic clay [18], core-shell type[11] . However, each of the above methods is not sufficient. We have suggested that ultrasonics could be used as the restricted reaction space for the synthesis [19] of the CdS compound. Acoustic waves with sufficiently high frequencies are applied to the solution. This can produce cavitations that have restricted reaction space and can break the bigger particles into many smaller ones. Moreover when certain conditions are used, the film is formed with a narrow size distribution. It is well known that high quality ITO films are easily obtained at high substrate temperature or with post-annealing [20-22]. Therefore an improvement of the method to grow ITO films at room temperature (RT) or without post-thermal treatment is needed for practical applications and industrial production. This is due to the fact that many materials do not sustain high process temperatures in multilayer structures [22-25]. Until now many deposition technologies such as vacuum evaporation, sputtering, chemical vapor deposition, spray pyrolysis, and precipitation from an aqueous solution or chemical bath deposition (CBD) have been used to fabricate CdS [26-29]and ITO films. Among the techniques available for CdS and ITO thin film production, sputtering and CBD are the most widely studied, and large-scale deposition sets are available. In our previous study [3], RF diode sputtering with bias voltage was used for the deposition of ITO films without the need for substrate heating or post-annealing process. The CBD method was used for the CdS deposition with easy process, large area and low cost. Although the CBD method can produce CdS films with good electrical and optical properties, if big CdS colloidal particles or clusters precipitated in the solution, adsorb randomly to the surface in the growing film, this leads to an opaque CdS film with poor uniformity and adherence.

In this chapter we present the study of the properties of CdS films on dc sputtered ITO produced with the ultrafine particle (UFP) structure, by the called "ultrasonic colloid deposition (USCD)". The reaction equation is $Cd^{2+} + S^{2-} = CdS$, the detail forming process of the CdS and reaction mechanism of the CdS are referenced to our previous report [3]. We propose and discuss a bilayer film model, in which if both CdS and ITO layers are thin enough, the effect of the interface is strong and the final behavior is similar to the doped material. In addition dc sputtered ITO and dipped CdS films are known to be amorphous. These characteristics make them suitable for applications and match with the

amorphous WO_3 films in ECDs.

6.2. Sheet Resistance

In chapter 4 the lower sheet resistance (R_s) value of the ITO films is 85.6 Ω/Sq (Sample-d2, thickness: 188 nm, 10% P_{O2}). The resistivity of as-deposited ITO film is sufficiently low to use it as an electrode layer. The value of R_s of an as-deposited CdS film (thickness: 450 nm) on ITO (188 nm) was 670 Ω/Sq while for as-deposited CdS films on glass was 10^8 Ω/Sq by CBD and 10^6 Ω/Sq by vacuum deposition. The R_s of the film decreases after annealing it from 100 ^{0}C to 300 ^{0}C in $N_2 + 5\%H_2$. The electrical measurements showed that the resistivity of a CdS/ITO film is much better than that of the CdS film itself.

6.3. Transmission of the Films

Since the transmission data can give easily optical parameters information [11, 30-31], the transmission spectra were measured in order to visualise the absorption onset. Three optical transmission spectra of the CdS films, prepared vacuum evaporation, chemical bath deposition (CBD) and USCD method, are shown in Fig. 6-1. The transmittance increases and the transparent spectral range is broadened for CdS using the USCD method. It is also found that the onset of the spectrum using the USCD method is located at 480 nm and it is shifted towards shorter wavelengths by 30 nm from the vacuum deposited value of 510 nm. The slope of the edge of the transmission curve is steep, in accordance with a narrow distribution of particle sizes. The absorption peak (transmission onset) is due to a 1s-1s quantum particle transition as suggested by Brus [13, 32]. This can be related to the formation of an UFP film and the increase in their crystalline nature associated with the decrease in the defect concentration (Ref. Section 4.2.1).

The transmission spectra of the ITO films as deposited and annealing in vacuum are shown in Fig. 4-5-1 and Fig. 4-6-3 of Chapter 4. A maximum transmission of about 99 % is achieved in the visible region after annealing in vacuum. The transmittance of ITO increases with increasing annealing temperature. The domain, thickness of thin film and crystalline/defect ratio become larger after annealing, but there are still some small UFP sizes inside the large domain of the film.
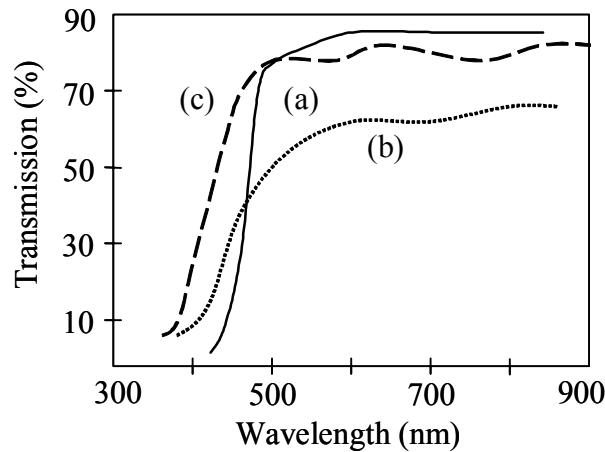
Fig. 6-1. The transmission of CdS films: (a) using a vacuum evaporation method; (b) using a chemical bath deposition (CBD) method; (c) using an USCD method.
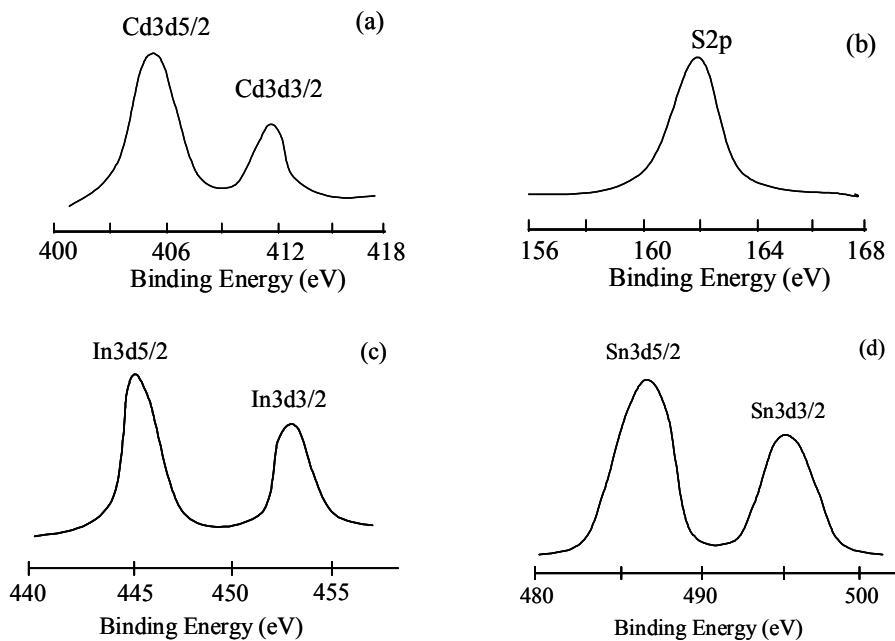

Fig. 6-2. XPS spectra of CdS on Cd3d (a) and S2p (b); XPS spectra of ITO on In3d (c) and Sn3d (d).

6.4. XPS Study of the Films

Fig. 6-2 shows the XPS spectra of CdS and ITO films. Fig. 6-2 (a) represents the XPS signature of the Cd 3d doublet (3d $_{5/2}$ and 3d $_{3/2}$). High-resolution scans from 400.0 eV to 418.0 eV revealed the $3d_{5/2}$ peak at 404.3 eV and the $3d_{3/2}$ peak at 411.2 eV. A high-resolution scan from 156.0 eV to 168.o eV revealed the S2p peak at 161.9 eV (Fig. 6-2 b). The peak positions, line shapes, and peak-to-peak distance of the Cd_{3d} doublet and

S2p confirmed that the deposited film contain CdS. The XPS spectra near the In3d peak and Sn3d doublet are shown in Fig. 6-2(c) and (d) respectively. They show only one binding state for In and Sn since there is no sign of broadening or splitting of the peaks. The XPS spectra indicate that the oxygen is bonded to the indium and tin. The binding energy of $In3d_{5/2}$ at 445.1 eV from Fig. 6-2c can be attributed to the In^{3+} bonding state of In_2O_3. The binding energy of $Sn3d_{5/2}$ is at 487.1 eV and corresponds to the Sn^{4+} bonding state of SnO_2. XPS analysis showed the formation of ITO film.

6.5. GIXRD Study of CdS/ITO Bilayer

In order to study the interface of CdS/ITO bilayer, we show the GIXRD (grazing incidence X-ray diffraction) results obtained on three samples in Fig. 6-3. They are CdS (450 nm)/ITO (846 nm, sample-d5), CdS as-deposited on glass and CdS/ITO annealed in gas ($5\%H_2+N_2$) at 300 ^{0} C. The annealing time was 15 minutes. GIXRD spectrum for the film of CdS/ITO on glass (no heat treating) at different incidence angles ($\alpha= 0.40 ^0- 5.00 ^0$) is given in Fig. 6-3 (a). Three diffraction peaks associated with CdS are at 26.5 ^{0}, 43.9^0 and 52.8^0. Four diffraction peaks associated with ITO ($In_2Sn_2O_{7-x}$) are at 30.5 ^{0}, 35.5^0, 50.9^0 and 60.5^0. The diffraction lines reveal the existence of an interfacial embedding between CdS and ITO even if the films are not annealed. GIXRD spectra for the annealed film of CdS/ITO are given in Fig. 6-3 (b). The corresponding ITO peaks of CdS/ITO bi-layer film disappear at low incidence angles ($\alpha=0.40 ^0$) after annealing. We can then conclude that the CdS layer on ITO becomes a good polycrystalline thin film. Since the corresponding ITO peaks of the annealed CdS/ITO film show higher intensity than that of unheated CdS/ITO film at incidence angles ($\alpha=0.90 ^0- 5.00 ^0$), it is concluded that the ITO becomes polycrystalline film too. It shows that the effect of interfacial embedding between CdS and ITO layers depends on the thickness of the layers. If both the CdS and ITO layers are thin like it is reprented in Fig. 6-4a, the effect of the interface is strong and the final behavior is similar to the doped material. If both CdS and ITO layer are thick or like in Fig. 6-4b, the effect of the interface can be neglected.

GIXRD spectra for the unheated CdS film on glass, at different incidence angles ($\alpha= 0.20 ^0- 2.00 ^0$) are given in Fig. 6-3 (c). The diffraction lines reveal the existence of CdS from the surface ($\alpha=0.20 ^0$) to the bottom ($\alpha=2.00 ^0$) of the film. The X-ray penetration depth is calibrated from 25 nm to 480 nm, when the incidence angles varied from 0.20 ^{0}- 5.00 ^{0}. The CdS peaks that appear at incidence angles $\alpha=5.00 ^0$ (Fig. 6-3 a) and $\alpha=2.00 ^0$

(Fig. 6-3 c) show that the thickness of the CdS films (the X-ray penetration depth) is ~ 500 nm and ~ 210 nm respectively. It is in agreement with the thickness measured by Ellipsometry.
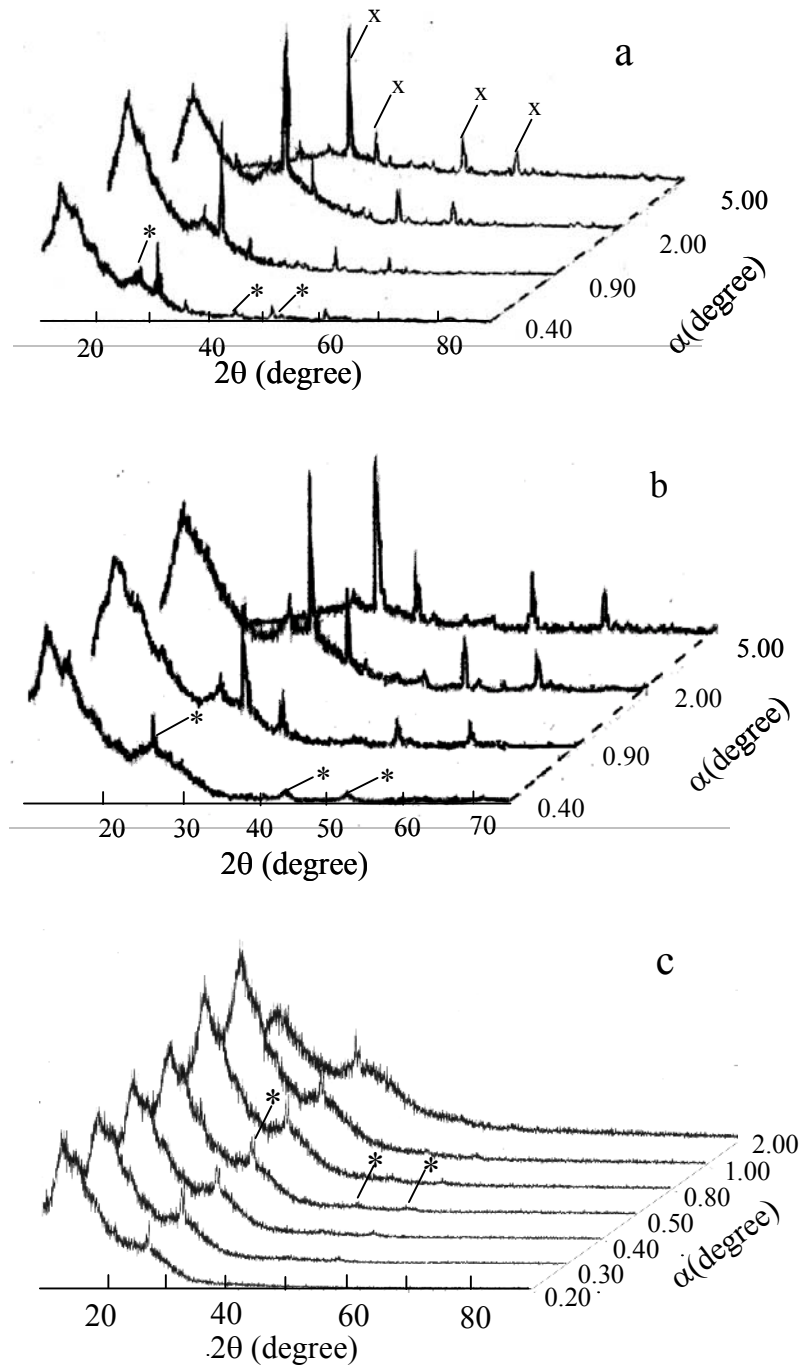

Fig. 6-3. Grazing incidence X-ray diffraction (GIXRD) at different incidence angles. (a) CdS/ITO (sample-d5); (b) CdS/ITO annealed in gas (5%H_2+N_2) at 300 ^{0}C for 15 minutes; (c) CdS as deposited. Symbol x – ITO ($In_2Sn_2O_{7-x}$); Symbol * - CdS.
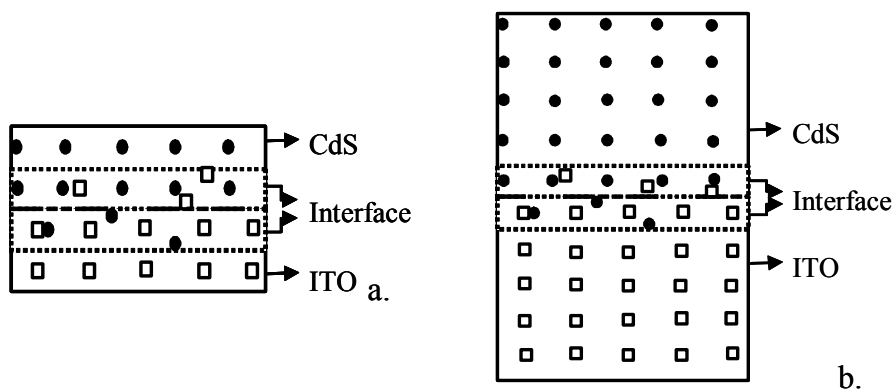
Fig. 6-4. The models of interfacial embedding between CdS and ITO (a): both CdS and ITO layers are thin (b): both CdS and ITO layers are thick (bulk)
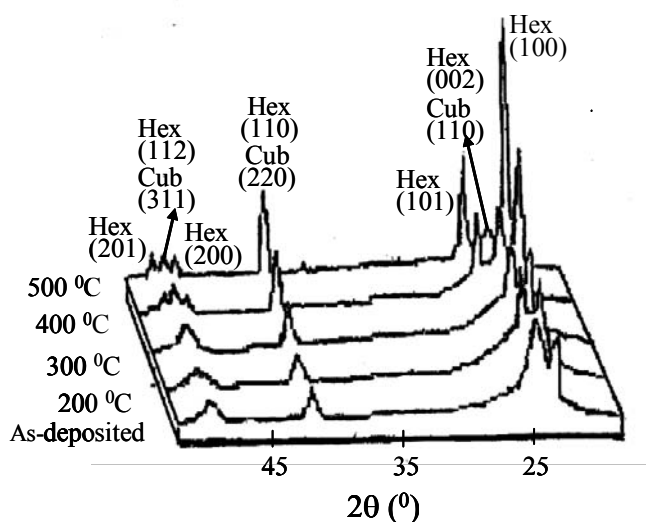

Fig. 6-5. The X-ray diffraction (XRD) of the CdS films at different annealing temperatures. Intensity is Arb. units

6.6. XRD of the Films

Fig. 6-5 shows the XRD of the CdS films deposited at different annealing temperatures. Polycrystalline hexagonal and cubic CdS are present showing many strong X-ray diffraction peaks. The diffraction spectra were obtained by using scanning of 2θ in the range 20^0 - 55^0. It can be seen that the as-deposited film has a mixed cubic and hexagonal forms of CdS. The peak at $2\theta=24.8^0$ corresponds to the hexagonal (100) plane, the peak at $2\theta=26.5^0$ corresponds to the mixture of hexagonal (002) and cubic (110) planes. The

peaks at $2\theta=43.9^0$ come from the hexagonal (110) and cubic (220) planes and the peak at $2\theta=52.8^0$ corresponds to the hexagonal (112) and cubic (311) planes. When the annealing temperature was increased to 400 ^{0}C, the peaks at $2\theta=28.2^0$, 50.8 ^{0} and 52.8^0, which come from the hexagonal (101), (200) and (201) planes, appeared. At the same time, the height of the peak at $2\theta=26.5^0$ decreased and the peak at 43.9 ^{0} increased. This indicates that the increase of the hexagonal structure content starts at 400 ^{0}C which is 100 ^{0}C lower than the Hiroshi Uda's results [17].

A typical X-ray diffraction pattern of the ITO film deposited on a glass substrate at different annealing temperatures is shown in Fig. 4-7-3 of Chapter 4. After annealing in air at 300 ^{0}C for 1 hour, the sharp (222), (211), (400), (440) and (622) peaks of In_2O_3 emerged on the XRD.
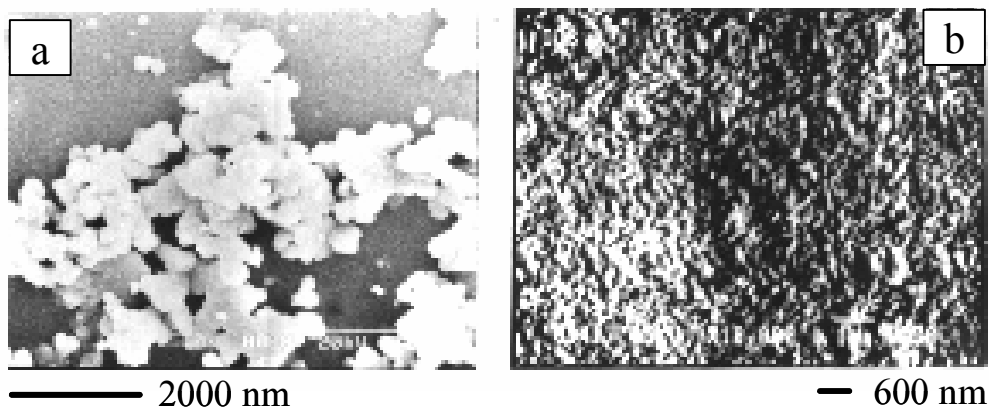

—— 2000 nm   — 600 nm

Fig. 6-6. (a) SEM image of CdS film deposited using the CBD method at 20kV. (b) SEM image of CdS film using the USCD method at 15kV.

6.7. Morphology of ITO and CdS Films

Surface roughness (δ) is an important parameter of the thin films. The data corresponding to the standard deviation of the microgeometric surface height was calculated from the total integrated scattering (TIS) [33]. Fig.4-5-5 of chapter 4 is a typical AFM micrograph of the surface microstructure of the ITO film. The surface roughness and nanometer grain boundaries are clearly seen in Fig. 4-5-5. Average grain size is 32 nm, the average height of δ is less than 16 nm.

The poly-crystal particle in the film could crumble by the ultrasonic vibration during the deposition. Even the deposition time of USCD was more than 50 minutes, it was still observed that the CdS film is quasi nanostructured and it presents a smooth surface. Fig.

6-6 (a, b) shows the SEM surface of the CdS on the ITO glass. Fig. 6-6a shows the SEM micrograph of a sample deposited by CBD method (no ultrasonics) in the temperature of 90 ^{0}C and pH of 11.8, in which the relevant deposition time is 9 minutes. There are big clusters of the colloids on the surface of the film.

From the Fig. 6-6b the SEM image shows that the CdS film on ITO is homogeneous and has high compactness. The adhesion of the CdS on ITO was found to be excellent and was checked by using the tape test. Also the films are composed of a single condensed layer of good quality and have a surface texture which can only be obtained by chemical etching [34]. It is easy to fix an upper limit of less than 300 nm in the length of the bar-shaped particles. The particles have a typical bar diameter of 100 nm. The microstructure and mechanism of film formation will be further discussed in the Section 6.8.

6.8. Mechanism of the Film Growth

6.8.1. Basic Models of Thin Film Growth

In both chemical and physical film growing, the nucleation, growth of the nuclei and coalescence of the separate islands are important for the formation of the film, i.e., the size of crystallites, orientations, and so on. Principally three different models of thin film condensation can be distinguishable as shown in the schematic illustration (Fig. 6-7) [35, 36], depending on the strength of the interaction between the atoms of the growing film and the substrate.

(a) Three-dimensional nucleation, forming and coalescence of islands (Volmer-Weber mechanism). Island growth occurs when the smallest stable clusters nucleate on the substrate and grow in three dimensions to form islands. This happens when atoms or molecules in the deposit are more strongly bound to each other than to the substrate.

(b) Layer-by-layer growth (van der Merwe mechanism). The layer growth appears when the extension of the smallest stable nucleolus occurs overwhelmingly in two dimensions. It results in the formation of planar sheets. In this growth mode the atoms are more strongly bound to the substrate than to each other. The first complete monolayer is then covered with a somewhat less tightly bound second layer. Providing the decrease in bounding energy is continuous towards the bulk crystal value, the layer growth mode is sustained. The most important example of this growth mode involves single crystal

epitaxial growth of semiconductor films.

(c) Adsorption of monolayer and subsequent nucleation on top of this layer (Stranski-Krastanov mechanism). The layer plus island growth mechanism is an intermediate combination of the above mention of modes. In this case, after the formation one or more monolayers, the subsequent layer growth becomes unfavourable and islands form. The transition from two-dimensional to three-dimensional growth is not completely understood, but any factor that disturbs the monotonic decrease in the binding energy characteristic of layer growth may be the cause. For example, due to film-substrate lattice mismatch, strain energy accumulates in the growing film. When released, the high energy at the deposit-intermediate layer interface may trigger island formation. This growth mode is fairly common and has been observed in metal-metal and metal-semiconductor systems.
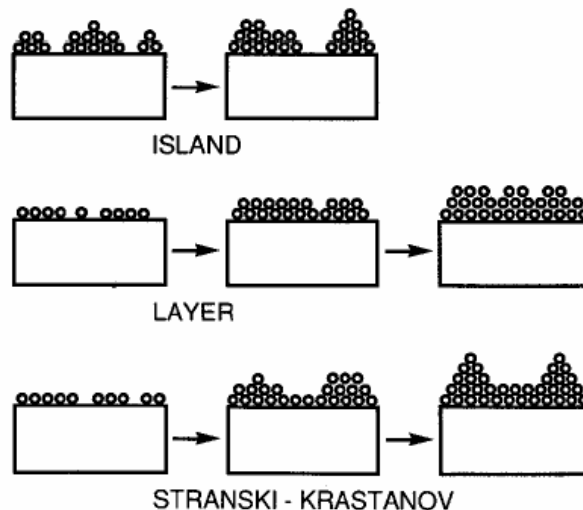

Fig. 6-7. Three basic models of thin film growth[35].

6.8.2. Thermodynamic (Capillarity) Theory of Nucleation

When the evaporated or sputtered particles reach the substrate, on which a thin film is to be deposited, they generally lose part of their energy on impingement. They are then attracted to the surface by forces mostly of dipole or quadrupole character and so they become adatoms that are adsorbed on the surface. Based on thermodynamic concepts and stems from the Langmuir-Frenkel theory of condensation [36, 37], we assume that the condensation nucleus has spherical shape with radius r. During its growth, by joining of additional particles (mostly by surface-diffusion), the nucleus energy consisting of the surface and volume component will change. Gibbs's free energy (free enthalpy or

Gibbs's potential ΔG_o) can then be written as:

$$\Delta G_o = 4\pi r^2 \sigma_{cv} + \frac{4}{3}\pi r^3 \Delta G_v \qquad (6.8.1)$$

where σ_{cv} is the condensate-vapour interfacial free energy and ΔG_v is the free-energy difference per unit volume of the phase of molecular volume V, condensed from the supersaturated vapour with the equivalent pressure, p, to the state with the equilibrium pressure p_e, i.e.,

$$\Delta G_V = -\frac{kT}{V}\ln\frac{p}{p_e} \qquad (6.8.2)$$

Fig. 6-8 shows the dependence of ΔG_o on the radius of the nucleus. It can be seen that this dependence possesses a maximum at a certain critical radius r^* which can be calculated from the condition

$$\frac{d(\Delta G_o)}{dr} = 0 \qquad (6.8.3)$$

The r^* value (i.e., radius of the critical nucleus) is therefore

$$r^* = -\frac{2\sigma_{cv}}{\Delta G_v} = \frac{2\sigma_{cv}V}{kT\ln\dfrac{p}{p_e}} \qquad (6.8.4)$$
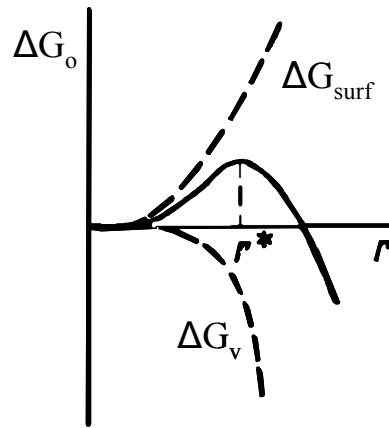

Fig. 6-8. The dependence of ΔG_o on nuclear radius

If the radius of the nucleus is smaller than r^*, the nucleus is unstable and there is a high probability that it will disintegrate (the nucleus tends to occupy the lowest energy state, which in this case requires disintegration into individual island atoms). If the radius is greater than r^*, the energy will decrease with increasing radius so the aggregates will grow until a continuous film is established. We can understand from this how important

for film formation is the ratio p/p_e, i.e., the supersaturation coefficient.

6.8.3. Growth and Coalescence of Islands

For reaching the final structure of the film further stages of growth are important. After nucleation it begins to fall into a process of individual island growth, and coalescence of the islands. Growth occurs mainly by surface diffusion of absorbed atoms and their attachment to the surface of the already existing nuclei.

The coalescence of film formation can proceed in three ways as shown in Fig. 6-9.

(a) Ostwald ripening: because of the difference in vapour pressure above small particles of different radii, a large nucleus will grow at the expense of a smaller one, till eventually the smaller one will completely disappear. This process is rather slow and is more important for annealing of the film after deposition than during deposition.

(b) Coalescence due to mobility of islands: the smaller nuclei are, as a rule, more mobile than the larger ones. Probably these processes are also slow to have influence during deposition (with exception of the mobility of atom pairs). These processes were investigated by Skoffronic, Venables et al.[38-39].

(c) Coalescence by growth: if two growing particles touch each other, they can –depending on the substrate temperature and the surface energies—either retain their shape almost completely, which corresponds to a sintering (agglomeration), or they can (mainly at higher temperatures) show a liquidlike behaviour and coalescence into a single one as can be seen in Fig. 6-10.
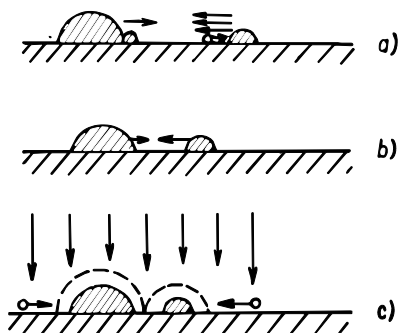

Fig. **6.9**. Coalescence mechanisms (a) Ostwald ripening; (b) cluster mobility; (c) coalescence by growth.
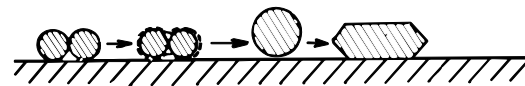
Fig. **6-10**. Coalescence of the islands and subsequent crystallisation.

The islands behave during coalescence like two droplets. The large interfacial energy of the system (isolated islands) decreases in the process. The nuclei growing on a

substrate may have different crystallographic orientations and conditions for growth. Large islands grow faster and small ones partially disappear due to the coalescence with larger ones. At each instant there is a certain size distribution (Gaussian) of the islands [40]. An interesting phenomenon is that in some cases the islands assume a crystallite shape but behave as a liquid during the coalescence process, after which a new crystallite is formed. It is believed that certain energy is liberated by coalescence that is sufficient to cause a temporary melting of the crystallites in contact. After coalescence the temperature drops and the born (new) island again crystallises. It has been established that when two islands of different sizes and crystallographic orientations coalesce, the resultant crystallite assumes the orientation of the large one.

The theory has enabled us to understand certain basic laws governing thin film formation and has provided a qualitatively correct idea about the influence of the particular factors on the initial stage of thin film growth. Its deficiency lies on the fact that it employs thermodynamic concepts and quantities that are applicable to microscopic systems. Even if this theory was developed from the heat evaporation process, it was also suitable for the nucleation stage of the solution and sputtering process of the film growth.

6.8.4. Influence of Substrate Temperature and Sputtering Pressure (Thornton Model)

As we have discussed, condensation from the vapour involves incident atoms becoming bonding adatoms, which then diffuse over the film surface until they are trapped at low-energy lattice sites or desorbed. Finally, incorporated atoms reach their equilibrium position in the lattice by bulk diffusion motion. This atomic odyssey involves four basic processes: shadowing, surface diffusion, bulk diffusion, and desorption. So, more specifically, the adatom mobility is an important factor on the structure during the film growth. The main parameters for the effect of the adatom mobility are the substrate temperature and particle bombardment [41-43].

The zone diagrams of Movchan & Demchishin and Thornton are useful tools for semi-quantitatively capturing and illustrating the expectations for structural evolution as a function of the process parameters, deposition temperature, and pressure. The microstructures of the films are usually classified in terms of four zones (Fig. 6-11) [44, 45]. Zone 1 structure, consisting of trapered columns and significant voids between columns, is prevalent in which the ratio T/T_{mp} is less than 0.3, where T is the growth temperature and T_{mp} is the melting point of the deposited material. In this range of growth temperature

adatom diffusion is negligible and, as a result of shadowing effects, most of the sputtered flux is deposited on high points on the film, with little material reaching the valleys. Zone 1 structure tends to be associated with rough surfaces, poor stability, and properties that are far from those of the bulk material [46].

Zone 2 is usually found when $0.3<T/T_{mp}<0.5$, which is associated with significant adatom diffusion on grains surface. Zone 2 structure is characterised by columnar, platelet, or whisker grains separated by dense intercrystalline boundaries.

Zone 3 occurs at high relative temperatures, $T/T_{mp} >0.5$, when diffusion within the grains is a significant mechanism of film growth. Zone 3 is associated with equiaxied grains and epitaxial on the substrate.

The fourth zone, Zone T, is the result of bombardment induced surface mobility. Films that would have been expected to be Zone 1 structures on the basis of T/T_{mp} can be grown with a very smooth surface and high density by bombarding the growing film with energy particles during growth [45, 47-49].
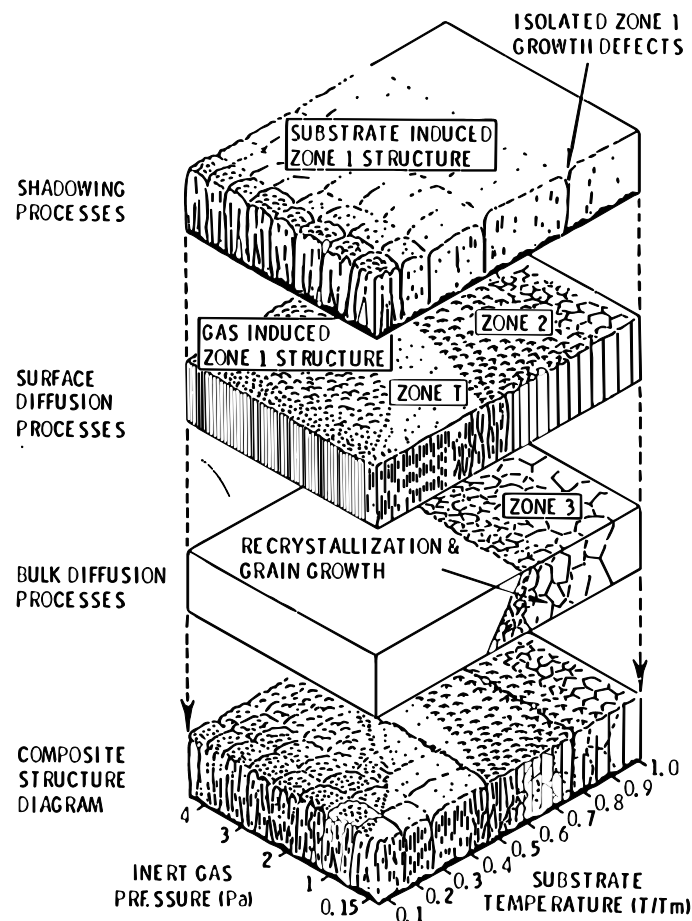

Fig. 6-11. Schematic representation showing the superposition of physical processes which establish the structure zones.

In addition we noted that a higher substrate temperature and a low deposition rate lead to an increase in the size of the grains. The statement is confirmed by the comparison of the ITO films sputtered at RT and 400 ^{0}C substrate temperatures in the AFM photographs of Fig. 4-2-3 and Fig. 4-4-3 (Chapter 4). The comparison of V_2O_5 films, which were deposited at RT and 400 ^{0}C T_s, is another example (Section 8.9).

6.8.5.   Morphology and Mechanism of Formed CdS Films

The growth of CdS film may be assigned to "Island Growth" (Section 6.8.1). In CBD and USCD growing methods, a cadmium complex (ammonia, triethanolamine) and an organic sulfidizing agent (thiourea or thioacetamide) provides a concentrations of Cd^{+2} and S^{-2} in the solution. When the product of the ion concentration of Cd^{+2} and S^{-2} exceeds the solubility product of CdS, a chemical precipitation takes place. Firstly there would be an actual inception of submicroscopic nuclei, growth of the submicroscopic nuclei, and an ion-by-ion reaction that takes place at the solid- liquid interface (called stage 1). It is generally assumed that solutions in the supersaturated state constitute micro heterogeneous systems in the form of a solution of suspended crystal subnuclei. Secondly when the deposition time is prolonged, the cluster-by-cluster (colloid-by-colloid, called stage 2) growth in the solution and on the substrate, whereby clusters coalesce through an attractive force (probably van der Waals), occurs. The growth of these nuclei to a certain equilibrium size by diffusion and flowage is scarcely probability. It is entirely possible by virtue of their convergence and subsequent coalescence into clustered aggregates, which become larger particles due to the tendency of decreasing of Gibbs's free energy (Section 6.8.2). The formation of a large number of clusters in the two-phase solidification zone inhibits the motion of nuclei and the liquid phase, because the canals between the cluster and dendrites can diminish to capillary dimensions. The CdS solidifies before the liquid phase enters the capillaries, resulting in the formation of pores and shrinkage cavities. The problem is that the two reactions of ion-by-ion and cluster-by-cluster are usually taking place at a very short time difference. It is difficult to inhibit the second stage to begin. The two stages were proved by our SEM micrographs [3] in the 73 ^{0}C temperatures and pH 11.0 condition.

In the USCD, the ultrasonics could inhibit the above second process. It resists the growth of the cluster pores. If we take into account of the fact that dendrite formations are present at the instant of crystallization, we realize that they can be broken and cast into the solution by shaking, vibration or ultrasonic irradiation. The breakdown of the

dendrite branches under vibration tends to eliminate the pores and shrinkage cavities in the solidifying CdS. The polycrystalline particles suspended in the film could also be cut or ground by the vibrating medium during the deposition. Even if the deposition time of USCD was more than 50 minutes, it was still observed that the CdS film was quasi nano-structure and has a smooth surface. Fig. 6-6 shows the SEM micrographs of the surface of the CdS films that were produced by traditional CBD method and USCD method. It supports the above explanation.

6.8.6. Function of Ultrasonic Cavitations

If we try to deduce why the USCD method can produce that kind of micro-structured films, the ultrasonic cavitation has to be introduced. Ultrasonic waves are mechanical pressure waves formed by actuating the ultrasonic transducer with high frequency. A typical ultrasonic power generator produces waves in frequency range 20-120 kHz. Typical ultrasonic transducers are normally mounted on the bottom and/or the sides of the tanks or immersed in the liquid. The generated ultrasonic waves propagate perpendicularly to the resonating surface. The waves interact with liquid media to generate cavitation implosions. High intensity ultrasonic waves create micro vapor/vacuum bubbles in the liquid medium (Fig. 6-12), which grow to maximum sizes proportional to the applied ultrasonic frequency and then implode, releasing their energies. The higher the frequency is, the smaller the cavitation size has.

The ultrasonic model illustrates the generating cavitations through at least three steps: nucleation, growth and violent collapse or implosion. The transient cavities (or vacuum bubbles or vapor voids), ranging 5-150 microns in diameter, are produced during the sound waves' half cycles. During the rarefaction phase of the sound wave, the liquid molecules are extended outward against and beyond the liquid natural physical elasticity/bonding/attraction forces, and then the generated vacuum nuclei continue to grow. A violent collapse occurs during the compression phase of the wave. Cavitations are generated in the order of microseconds. At the 20 kHz frequency, it is estimated that the pressure is about 35-70 K Pascal and the transient localized temperatures are about 5000ºC, with the velocity of micro streaming around 400 Km/hr [50] .

In an ultrasonic field (42 kHz) the reaction space of CdS can be refined in the micro ellipsoid volume-cavitation (Fig. 6-12). We deduced that the bar-shaped CdS is following the shape of an acoustic cavitation generated by the sound field after the sound wave was transferred and focused from sound source to bath. The cavitation plays a vital

part in the peptizing method deposition action of the ultrasonic method. The effect of high pressure and high temperature in the cavitation of the ultrasonic liquid makes the formation of bar-shaped CdS UFP film. In next part- Section 6.8.7, effect of high temperature and other fields for the formation of bar-shaped volume will be focused. This film has good transparency and is highly adhesive. In addition during the CdS deposition, the ultrasound produces microturbulence at the bounding surfaces and accelerates the mass transfer of matter from one phase to another phase.

Fig. 6-12. Photograph of a collapsing cavitation bubble. Width of the bubble is approximately one mm. from University of Washington, Applied Physics Laboratory (Lawrence Crum, Ph.D.)

6.8.7. Formation of Bar-shaped Structures

In general the particles are not always spherical shape. They can have different shapes. Their adhesive force can be van der Waals, electrical double layer, capillary and electrostatic. In theory these forces are directly proportional in magnitude to the size of the particle.

Summing-up the above Sections and other references [3, 35, 37] on mechanisms of film growth, the growing process of normal films can be divided into four stages as follows:

(i) Nucleation, during which small nuclei are formed that are statistically distributed (with some exceptions) over the substrate surface.

(ii) Growth of the nuclei and formation of larger islands, which often have the shape of small crystals (crystallites).

(iii) Coalescence of the islands (crystallites) and formation of a more or less connected network containing empty channels.

(iv) Growth of continuous film.

As we know sintering as well as film deposition of high temperature is a coalescence mechanism on neck (bar) forms involving islands in contact [51-52]. It can be understood in the TEM (transmission electron microscope) of Fig. 6-13, depicting a time sequence of coalescence events between Au particles deposited on molybdenite (MoS_2) at 400 ^{0}C.

Within tenths of a second a neck forms between islands and then successively thickens as atoms are transported into the region. The driving force for neck growth is simply the natural tendency to reduce the total surface energy (or area) of the system. Since atoms on the convex island surfaces have a greater activity than atoms situated in the concave neck, an effective concentration gradient between these regions develops. This results in the observed mass transport into the neck. Surface energy and diffusion-controlled mass-transport mechanisms influence liquid like coalescence phenomena involving islands in contact. Other driving forces such as electric field [51] and flowage field are probably also operative.
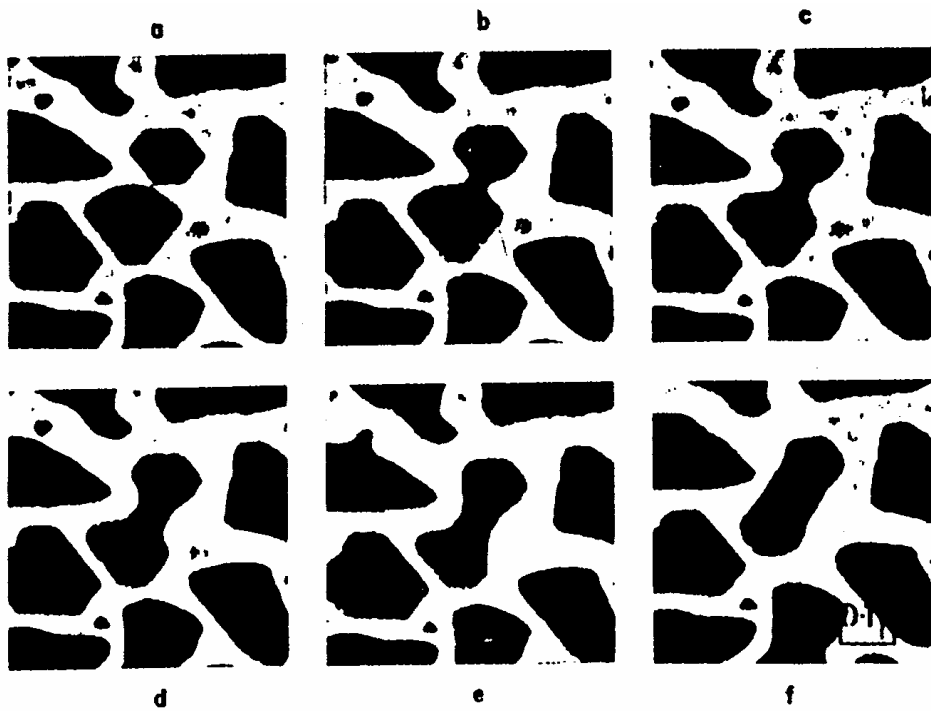

Fig. 6-13. Successive TEM of Au deposited on molybdenite at 400 ^{0}C illustrating island coalescence by sintering (a) arbitrary zero time, (b) 0.06 Sec., (c) 0.18 Sec., (d) 0.50 Sec., (e) 1.06 Sec., (f) 6.18 Sec[51].

As the example in the deposition process of the CdS films the driving forces come probably from the ultrasonic field. The final shape of the particles in Fig. 6-6b is bar (or neck) and not quasi sphere after prolonging the time of deposition further. It is also because the oriented ultrasonic progress (field) and flowage field limited the expansion or coalescence of Neck Island along the diametric direction of neck except mechanism of surface energy in heat field of high temperature.

Other examples are the deposition process of the ITO and V_2O_5 films in which the driving forces come possibly from combination of the oxygen flowing direction and heat

field of the high temperature. The final shape of the particle is quasi bar and not quasi sphere by the AFM of Fig. 4-4-3 in Chapter 4 and Fig. 8-9-6 in Chapter 8.

6.8.8. Conclusion of the Section

Principally three different models of film condensation are distinguishable, depending on the strength of the interaction between the atoms of the growing film and the substrate. They are (a) a three-dimensional nucleation, forming, and coalescence of islands (Volmer-Weber mechanism); (b) the layer-by-layer growth(van der Merwe mechanism); (c) adsorption of monolayer and subsequent nucleation on top of this layer (Stranski-Krastanov mechanism).

The discussion of thermodynamic (capillarity) theory of nucleation, growth/coalescence of islands in a film and microstructure were classified in terms of four Zones enabled us to understand certain basic laws governing thin film formation. They have provided qualitatively the correct idea about the influence of particular factors on the initial stage of thin film growth.

Four stages of the growing process of a film were discussed and given. They are (i) Nucleation, (ii) Growth of the nuclei and formation of larger islands, (iii) Coalescence of the islands (crystallites) and formation of a more or less connected network containing empty channels, (iv) Growth of continuous film.

The structure formation and mechanism of the film on ultrasonic dipped deposition and sputtering methods were discussed. Especially as examples, the CdS films grown by USCD, the ITO and V_2O_5 films sputtered at 400 ^{0}C substrate temperature were analyzed and the formation of a bar shaped structure was explained.

6.9. Summary of the Chapter

A CdS/ITO bi-layer film was deposited onto glass and quartz substrates assisted using both physical and chemical methods. The dipped CdS was grown through the ultrasonic colloid deposition (USCD) method. The USCD is a method to produce bar-shaped UFP film of cadmium sulfide at low cost and with easy process. This resulted in a dramatic difference in surface morphology, growing rate and optical properties of the CdS films. The main point of the technique is that by feeding the ultrasonic generator with a known concentration of ions, we can define the size of the chemical reaction space in the solution, break up the bigger particles, supply high pressure and super high temperature in the cavitations plus ultrasonic flowage field (Section 9.6 and 9.7), and hence define the size

of the final particles in the film.

The CdS film obtained using USCD has a wider transmission range, a higher transmittance and better uniformity than the CdS film obtained using the CBD method. XPS and XRD results confirmed that the dipped film is the CdS. USCD method can also be used in industry instead of a chemical etching step and directly obtain the surface texture and produce CdS films. The method could also be applied to other kinds of films and has potential for the production of UFP films.

The structural, electrical and optical characteristics of the bi-layer films were studied. The results demonstrate that the CdS films on ITO have much lower sheet resistance than a single CdS layer with the same thickness. The CdS/ITO bi-layer was investigated by means of XPS and XRD. The characterization of the bi-layer film from the CdS surface to the CdS/ITO interface, and then to the ITO bottom were studied by GIXD at different incidence angles ($\alpha = 0.20^0 - 5.00^0$). The diffraction lines reveal the existence of an interfacial intermixing between CdS and ITO even if the films are not annealed. If both CdS and ITO layers are thin enough, the effect of the interface is strong and the final behavior is similar to a doped material. In addition, dc sputtered ITO and dipped CdS films are known to be amorphous. These characteristics make them suitable for applications by matching with amorphous WO_3 layers in ECDs.

The discussion of thermodynamic (capillarity) theory of nucleation, growth/coalescence of islands in a film and microstructure were classified in terms of four Zones enabled us to understand certain basic laws governing thin film formation. Principally three different models of film condensation are distinguishable too. They have provided qualitatively the correct idea about the influence of particular factors on the stage of thin film growth. The structure formation and mechanism of the film on ultrasonic dipped deposition and sputtering methods were discussed. Especially as examples, the CdS films grown by USCD, the ITO and V_2O_5 films sputtered at $400\,^0C$ substrate temperature were analyzed and the formation of a bar shaped structure was explained.

6.10. References

[1]   K. Subbarramaiah, V. Sundara Raja, Solar Energy Materials and Materials and Solar Cells 32(1994)1.

[2]   D. Hariskos, M. Powalla, N. Chevaldonnet, D. Lincot, A. Schindler, B. Dimmler, Thin Solid Films 387 (2001) 179.

[3]   H.-N. Cui, S.-Q. Xi, Thin Solid Films 288(1996) 325.

[4]   S. Papaefthimiou, G. Leftheriotis, P. Yianoulis, Electrochimica Acta 46(2001) 2145.

[5]   M. Ristova, M. Ristov, Appli. Surf. Sci. 181(2001) 68.

[6]   Satyen K. Deb, S. H. Lee, C. Edwin Tracy, Pitts J. Roland, Brian A. Gregg, Howard M. Branz, Electrochimica Acta 46(2001) 2125.

[7]   J. Krustok, P. E. Kukk, Mater. Sci. 15(3) (1989) 43.

[8]   R. D. Shannon, J. L. Gillson, R. J. Bouchard, J. Phys. Chem. Solids 38(1977) 877.

[9]   D. R. Kammler, T. O. Mason, D. L. Young, T. J. Coutts, J. Appli. Phys. 90(7) (2001)3263.

[10] L. E. Brus, Appl. Phys. A53 (1991) 465.

[11] Y. C. Tian, T. Newton, N. A. Kotov, D. M. Guide, J. H. Fendler, J. Phys. Chem. 100(1996) 8927.

[12] J. H. Fendler, F. C. Meldrum, Adv. Mater. 7 (1995) 607.

[13] K. Rajeshwar, Adv. Mater. 4(1992) 23.

[14] M. Wu, W. J. Gu, W. Z. Li, X. W. Zhu, F. D. Wang, S. T. Zhao, Chem. Phys. Lett., 224(1994) 557.

[15] H.- N. Cui, R. Wang, W.-Y. Wang, S.-Q. Xi, J. of Materials Science Letters 17(11)(1998)913.

[16] J. Kuczynsk, J. K. Thomas, Chem. Phys. Lett. 89(1985) 2720.

[17] S. L. Suib, Chem. Rev. 93 (1993) 803.

[18] R. D. Stramel, T. Nakamura, J. K. Thomas, Chem. Phys. Lett. 130(1986) 432.

[19] H. N. Cui,. R. Wang, H. J. Zhang, L. Y. Wang, S. Q. Xi, China Patent December. The application and public No. 96123704x. 1996.

[20] A. L. Dawar, J. C. Joshi, Mater. Sci. 19(1984) 1.

[21] I. Hamberg, C. C. J. Granqvist, Appl. Phys. 60(1996)R123.

[22] T. J. Vink, W. Walrave, J. Daams, P. Baarslag, J. Jer. Meerakker, Thin Solid Films 266(1995) 145.

[23] P. Song, Y. Shigesato, I. Yasui, C. W. Yang, D. C. Paine, Jpn.J. Appl. Phys., Part 1 37(1998) 1870.

[24] C. G. Ganqvist, Solar Energy Material & Solar Cells 60(2000) 201.

[25] M. Bender, W. Seelig, C. Daube, B. Ocker, J. Stollenwerk, Thin Solid Films 326(1998) 72.

[26] O. Conde, A.G. Rolo, M.J.M. Gomes, C. Ricolleau and D.J. Barber, HRTEM and GIXRD studies of CdS nanocrystals embedded in Al_2O_3 films produced by magnetron rf-sputtering, Journal Crystal Growth, **247** (3-4) (2003) 371-380.

[27] Boev. V. I.; Silva, C. J R.; Gomes, M. J. M, Synthesis and characterization of a sol-gel derived ureasilicate hybrid organic-inorganic matrix containing CdS colloidal particles, J. of Sol-Gel Science and Technology, Vol. 31 (2004) p. 131-135.

[28]   T. D. Dzhafarov, M. Altunbas, A. I. Kopya, V. Novruzov, and E. Bacaksiz, Formation of p-type CdS thin films by laser-stimulated copper diffusion, J. Phys. D: Appl. Phys. 32 (24) (1999) L125-L128.

[29]   M. Rusu, A. Rumberg, S. Schuler, S. Nishiwaki, R. Wurz, S. M. Babu, M. Dziedzina, C. Kelch, S. Siebentritt, R. Klenk et al., Optimisation of the CBD CdS deposition parameters for ZnO/ CdS /CuGaSe2/Mo solar cells, Journal of Physics and Chemistry of Solids, 64(9-10)(2003) 1849-1853.

[30]   H. N. Cui, W. Y. Wang, E. L. Zhou, X. G. Zhao, Thin Solid Films 214(1992) 238.

[31]   F. O. Adurodija, H. Lzurni, T. Ishihara, H. Yoshioka, M. Motoyama, Influence of substrate temperature on the properties of indium oxide thin films, J. Vac. Sci. Technol. A 18(3) (2000)814.

[32]   L. E. Brus, IEEE. J. Quantum Electron 22(1986)1909.

[33] H.-N. Cui, V. Teixeira, Mechanics and Material Engineering for Science and Experiments (Editor: Zhao, Y. et al), Science Press, Sci. Press New York Ltd. (2001) 292.

[34]   J. X. Wang, Y. R. Sun, T. B. Li, Some improvements in thin film CdS/Cu2S solar cells, Acta Energiae Solaris Sinica 3(1)(1982) 37.

[35]   Milton Ohring, The Materials Science of Thin Films, Academic Press(San Diego, New York, London) (1992) P.197

[36]   J. L. Vossen, W. Kern, (eds.), Thin Films Processes I and II, Academic Press, New York, 1991.

[37]   B. Lewis and J. C. Anderson, Nucleation and Growth of Thin Films, Academic Press, London (1978)

[38]   J.A.Venable, Phil. Mag., 27 (1973) 697

[39]   H., J. Reiss, Appl. Phys., 39 (1968) 5045

[40]   J. Poeza, P. Barna, A. Barna, J. Vac. Sci. Technol. 6 (1969) 472

[41]   D.W.Hoffman, J.A.Thornton, J. Vac. Sci. Technol. 20 (1982) 355

[42]   P.Zeriman, E.Kay, . J. Vac. Sci. Technol. 21 (1982) 828

[43]   J.M.Harper, J.J.Cuomo, R.J.Gambino, H.R.Karfman, in" Ion Bombardment Modification of Surface: Fundamentals and Applications" (O.Aucillo, R.Kalley, eds). Elsevier , Amsterdam, 1984

[44]   J.A. Thornton, Ann. Rev. Mater. Sci. 7 (1977) 239

[45]   J.A. Thornton, . J. Vac. Sci. Technol. 11 (1974) 666

[46]   A.G.Dirks, H.J.Leamy, Thin Solid Films 47 (1977) 219

[47]   R.Messier, A.P.Giri, R.A.Roy, J. Vac. Sci. Technol. A2 (1984) 500

[48]   R.Messier, J. Vac. Sci. Technol.A4(3) (1986) 490

[49]   D.M.Mattox, G.J.Kominiak, J. Electronchem.Soc. 120 (1973) 1535

[50]   Sami Awad, http://www.crest-ultrasonics.com/, CREST ULTRASONICS Manufacturer.

[51]   R. M. German, Powder Metallurgy Science, Metal Powder Industries Federation, Princeton, NJ (1984)

[52]   D. W. Pashley, M. J. Stowell, J. Vac. Sci. Tech. 3, 156 (1966)